

## Chapter 7

### Magnetic Measurement

As the old adage says, “garbage in equals garbage out”; inaccurate input translates to inaccurate output. The key inputs to PMAC simulation are magnetic torques; thus the parameters which govern these torques must be accurately measured to ensure that the simulation results are trustworthy. This chapter describes measurement techniques for both the static magnetic moment  $\mathbf{m}$  and the hysteresis rods. First, the design of a Helmholtz cage for accurate magnetic measurements is described (Section 7.1). Next, the static magnet magnetic moment  $\mathbf{m}$  is measured (Section 7.2). A Helmholtz-cage-based hysteresis rod measurement method is described (Section 7.3); this method is capable of measurement in the presence of other magnetic materials which could degrade the dampening capabilities of a hysteresis rod.

#### 7.1 Helmholtz Cage

A Helmholtz cage is a set of six wire coils (two per orthogonal axis) which can be used to provide an arbitrary uniform field within the volume enclosed by the coils; the properties of the uniform field depend upon the cage dimensions and available current. The cage operates on the principle that a current-carrying wire will produce a magnetic field, and can be used to both cancel the inherent magnetic field and supply an arbitrary magnetic field. The use of two coils per axis allows for a uniform field to be generated between the coils. A Helmholtz cage was constructed to perform multiple magnetic measurements relevant to a PMAC system. The theory of a Helmholtz cage is presented, followed by the design of the cage and post-build test results.

### 7.1.1 Theory

The Helmholtz cage theory is based on manipulation of the Biot-Savart law: [81]

$$\mathbf{B} = \frac{\mu_0 n I}{4\pi} \int \frac{d\mathbf{l} \times \hat{\mathbf{r}}}{r^2} \quad (7.1)$$

where  $\mathbf{B}$  is the magnetic field vector,  $\mu_0$  is the permeability of free space,  $I$  is the current of the wire being analyzed,  $d\mathbf{l}$  is an infinitesimal current-carrying wire element,  $r$  is the distance from element  $d\mathbf{l}$  to the point of  $\mathbf{B}$  measurement,  $\hat{\mathbf{r}}$  is a unit vector in the direction of  $r$ , and  $n$  is the number of turns in the current-carrying wire. The Biot-Savart law is used to determine the axial magnetic field due to two coils perpendicular to a single axis. First, the on-axis field due to a single wire segment on one of the coils is determined. A single coil is shown in Figure 7.1a. Here  $a$  is one-half of the side length  $A$  and the point of measurement  $P$  lies in the center of the coil. The distance  $z$  is measured from the center of the two coils, thus the -Z coil lies at  $z = -h/2$ , where  $h$  is the distance between the coils. Integration variables are shown as  $l$  and  $\theta$ .

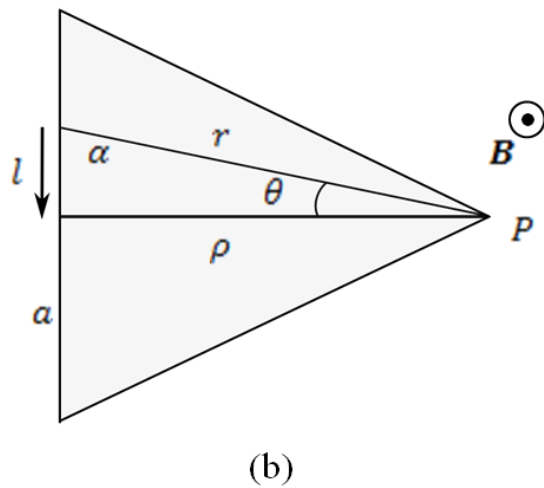
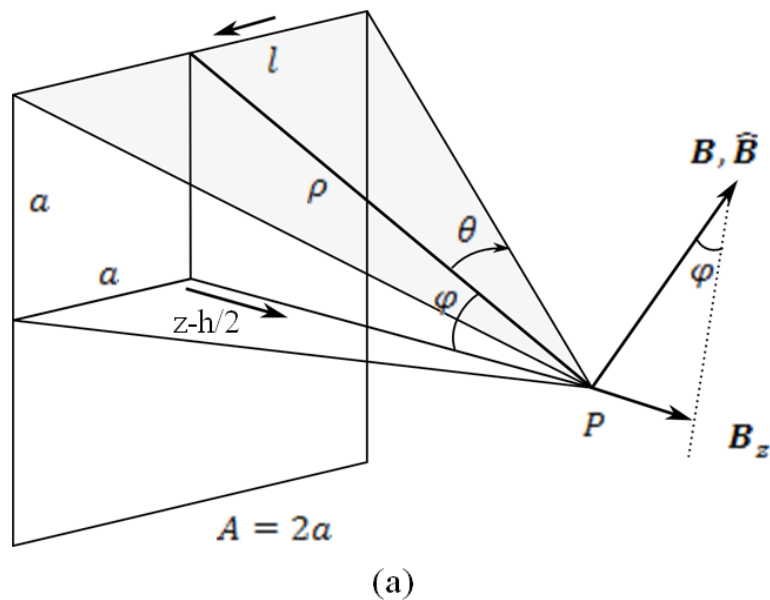
Figure 7.1b shows the relationships between the single wire segment and the field generated at on-axis location  $P$ . Note that the total field  $\mathbf{B}$  generated by the wire segment  $l$  is perpendicular to plane shown in Figure 7.1b. The trigonometric relationships shown in Figures 7.1a and 7.1b may be differentiated and combined with Equation 7.1 to arrive at Equation 7.2, which describes the infinitesimal magnetic flux generated by an infinitesimal length wire:

$$d\mathbf{B} = \frac{\mu_0 n I}{4\pi\rho} \cos \theta d\theta \hat{\mathbf{B}} \quad (7.2)$$

where  $\hat{\mathbf{B}}$  is the magnetic flux unit vector and  $\rho$  is the axial distance from the center of the wire segment to the point  $P$ . Equation 7.2 may be integrated from  $\theta_1 = -\sin^{-1}\left(\frac{a}{\sqrt{a^2+\rho^2}}\right)$  to  $\theta_2 = \sin^{-1}\left(\frac{a}{\sqrt{a^2+\rho^2}}\right)$  to yield Equation 7.3, the magnetic flux generated by a single length of wire of length  $2a$  as shown in Figure 7.1a. The direction of this field is perpendicular to the plane shown in Figure 7.1b:

$$B = \|\mathbf{B}\| = \frac{\mu_0 n I}{4\pi\rho} \left( \frac{2a}{\sqrt{a^2 + \rho^2}} \right). \quad (7.3)$$

Figure 7.1: Helmholtz geometry. (a) The -Z current-carrying coil and the resultant field generated at point  $P$ . (b) The generated field is perpendicular to the surface from the wire segment to point  $P$ .



When four wire segments of equal length are combined with the same current traveling in a counterclockwise direction (as shown in Figure 7.1a), it is apparent that only the contribution of the magnetic field perpendicular to the coil will remain. Thus, Equation 7.3 is multiplied by  $\sin(\phi) = \frac{a}{\rho}$  and a factor of 4 to yield the total axial field due to the -Z square coil:

$$B_{-z} = 4B \sin \phi = \frac{\mu_0 n I}{4\pi} \left( \frac{a}{\rho} \right) \left( \frac{2a}{\sqrt{a^2 + \rho^2}} \right) \quad (7.4)$$

where the direction of generated magnetic flux is given by the right hand rule based on the current flow. The field for the second coil can be calculated in much the same way, the only difference being  $\rho_{-Z} = \sqrt{z - h/2}$  and  $\rho_{+Z} = \sqrt{z + h/2}$ . Equation 7.5 gives the total field produced by both square coils as a function of axial distance  $z$  from the center of the coils:

$$B_z = \frac{\mu_0 n I}{\pi} \left( \frac{2a^2}{(a^2 + (z - h/2)^2) \sqrt{2a^2 + (z - h/2)^2}} + \frac{2a^2}{(a^2 + (z + h/2)^2) \sqrt{2a^2 + (z + h/2)^2}} \right). \quad (7.5)$$

### 7.1.2 Design

The Helmholtz cage was designed for the testing of CubeSat spacecraft. The following requirements governed the design of the Helmholtz cage:

- (1) The Helmholtz cage test volume shall have dimensions of 30cm×30cm×30cm.
- (2) The Helmholtz cage test volume shall provide 1% theoretical field uniformity along each axis.
- (3) The Helmholtz cage shall provide a magnetic field strength range of ±50 A/m on each axis.

The largest standard CubeSat is a 3U size, with dimensions 10cm×10cm×34cm [13]. Thus, requirement 1 ensures that the test volume is sufficient to measure any standard CubeSat (a 3U CubeSat easily fits when diagonally placed). Requirement 2 defines the expected uniformity of each axis of the Helmholtz cage. It is given in terms of theory because the empirical uniformity of each axis which may be measured by a magnetometer is dependent on the component of the earth

field along that axis. If the Helmholtz cage were placed in a magnetically noisy or non-uniform environment, the output field of the cage would be similarly noisy. However, a benefit of the small test volume is portability. If an environment is particularly noisy or non-uniform, the cage may be moved to a location that possesses a more stable field. Requirement 3 defines the configurable field within the Helmholtz cage after nullifying the earth-based local magnetic field.

In order to ensure these requirements were met, Equation 7.5 is used with various spacing between coils to determine the configuration that meets requirement 2. Figure 7.2 shows the results of this analysis. Spacing  $h$  is defined as the axial distance between the two coils of a single axis. The spacing  $h$  is given in terms of one half of the side length ( $a$ ). Thus, the analysis shown in Figure 7.2 is independent of cage size. The analysis shows that the best combination of uniform field and uniform distance is given by  $h = 1.2a$  which is the chosen spacing for the Helmholtz cage. Next, the side length of the Helmholtz cage is driven by requirement 1 above. In order to provide a 1% variation in field over a 30cm distance, the Helmholtz cage side length  $2a$  is set to 62.25cm and the coil spacing is set to  $h = 1.2a = 37.24\text{cm}$ . Figure 7.3 shows the normalized field resultant from these settings. The figure shows that along the axis from -15cm to 15cm, the theoretical flux density stays within 1% of the maximum value of the field, satisfying requirement 2.

There is a trade-off between the number of wire turns on each coil and the ability of the power supply to provide current to the coils. Each power supply has a maximum voltage and current it can deliver. The B&K Precision 9130 was chosen for use with the built Helmholtz cage, it has  $V_{max} = 30\text{V}$  and  $I_{max} = 3\text{A}$ . However, the relays which switch the polarity of the power supply output each have a current limit of  $I_{max} = 2\text{A}$ . As shown in Equation 7.5, the current through the coils  $I$  is directly proportional to the magnetizing field  $H$  within the Helmholtz cage. As the number of turns per coil increases, so does the resistance of each axis. Ohm's law shows that as the resistance  $R$  increases, eventually the power supply current will be limited by maximum voltage output  $V_{max}$ . For the B&K Precision 9130 power supply, the total resistance per axis must be less than  $15\Omega$  to allow the power supply to provide  $I_{max} = 2\text{A}$ . CSSWE's Helmholtz cage uses 30 turns of 22AWG magnet wire per coil, providing a total resistance of  $8.5\Omega$  per axis. Thus, the

Figure 7.2: The axial fields resultant of various coil spacings are shown. Here  $h$  is the axial distance between coils and  $2a$  is the side length of each square coil.

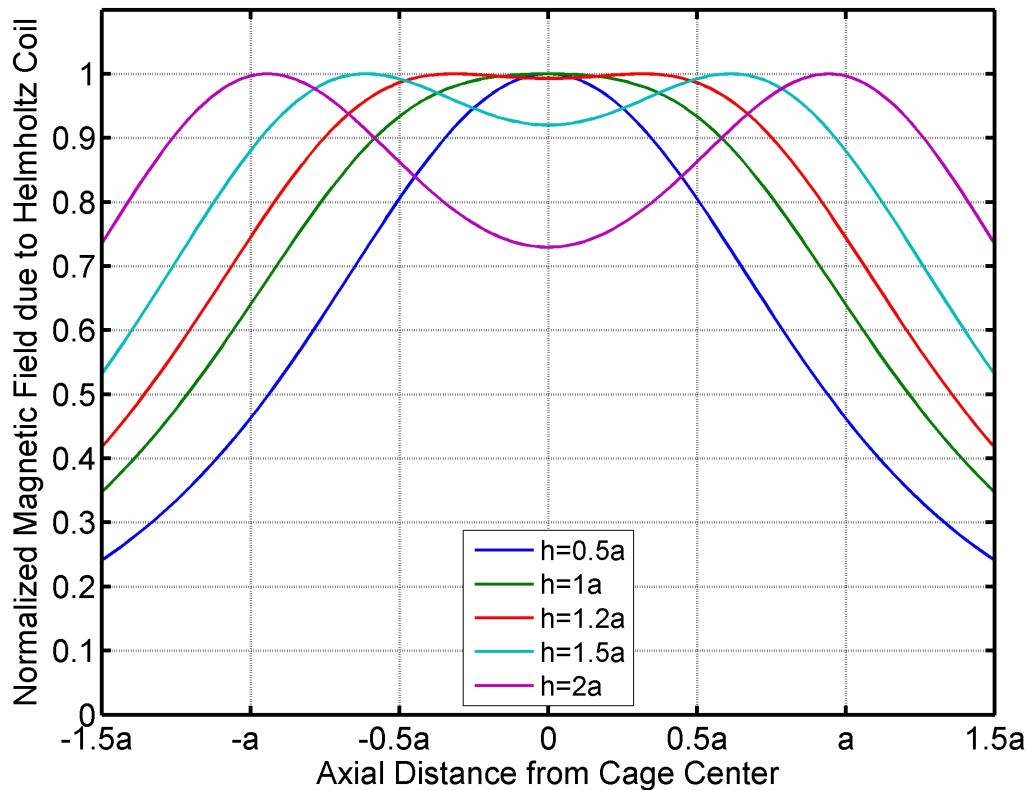


Table 7.1: All purchases needed to complete the Helmholtz cage are shown.

Part	Quantity	Cost (USD)
Acrylic walls (24in×24in×0.5in)	4	207
500ft. 22AWG magnet wire	3	73
B&K Precision 9130 computer-controlled 3-axis power supply	1	895
Micromag3 magnetometer	1	60
PIC18F452 QwikFlash microcontroller	1	132
BNC connectors	3	22
DPDT relays	3	15
<b>Total</b>		<b>1,404</b>

power supply can easily provide 2A of current to each axis. Using Equation 7.5 with  $I = 2\text{A}$  yields  $B_z > 125 \mu\text{Tesla}$  ( $H_z > 100 \text{ A/m}$ ) for  $-15\text{cm} < z < 15\text{cm}$ . The maximum earth-based magnetic field magnitude at the University of Colorado ( $40^\circ\text{N}$ ,  $105^\circ\text{W}$ , 1655m elevation) is  $< 40 \text{ A/m}$ . Thus, even with the worst-case alignment the Helmholtz cage is able to provide a magnetic field strength of at least  $60 \text{ A/m}$  per axis, satisfying requirement 3.

### 7.1.3 Assembly

Table 7.1 shows the parts needed to complete the Helmholtz cage setup; the total hardware cost is about \$1400 with the vast majority of that cost being the computer-controlled power supply. The Helmholtz cage construction began by assembling the 0.5 in. thick acrylic walls. The top and bottom of the cage were left open to allow access to the interior volume. Next, plastic guide rails and wooden spacers were added to ensure all coils are tight and square. Magnet wire was then wrapped around each axis one coil at a time, with care to ensure that both coils were wrapped in the same direction. Wooden legs were added to keep the cage weight off the magnet wire coils. Finally, BNC connectors were added to each axis for ease of connection to the power supply. Figure 7.4 shows the finished Helmholtz cage.

Figure 7.3: The theoretical axial magnetic field of the as-built Helmholtz cage with a spacing of  $h = 1.2a = 37.24\text{cm}$ . The magnetic flux density  $B$  is normalized by the maximum flux density.

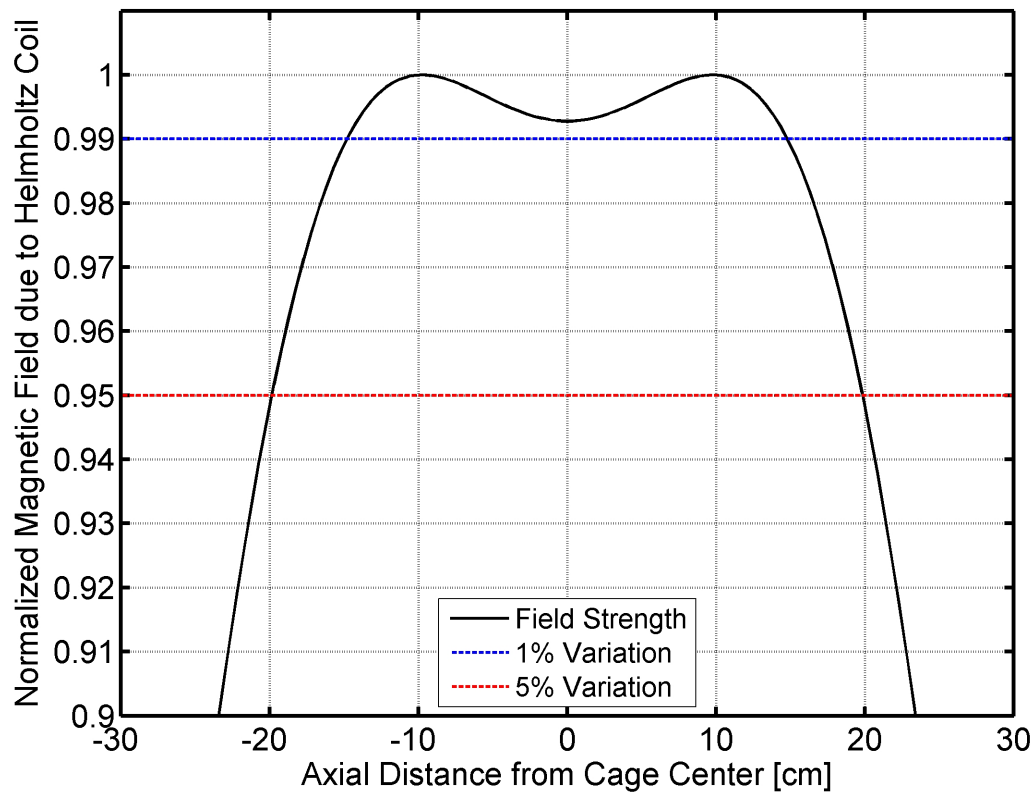
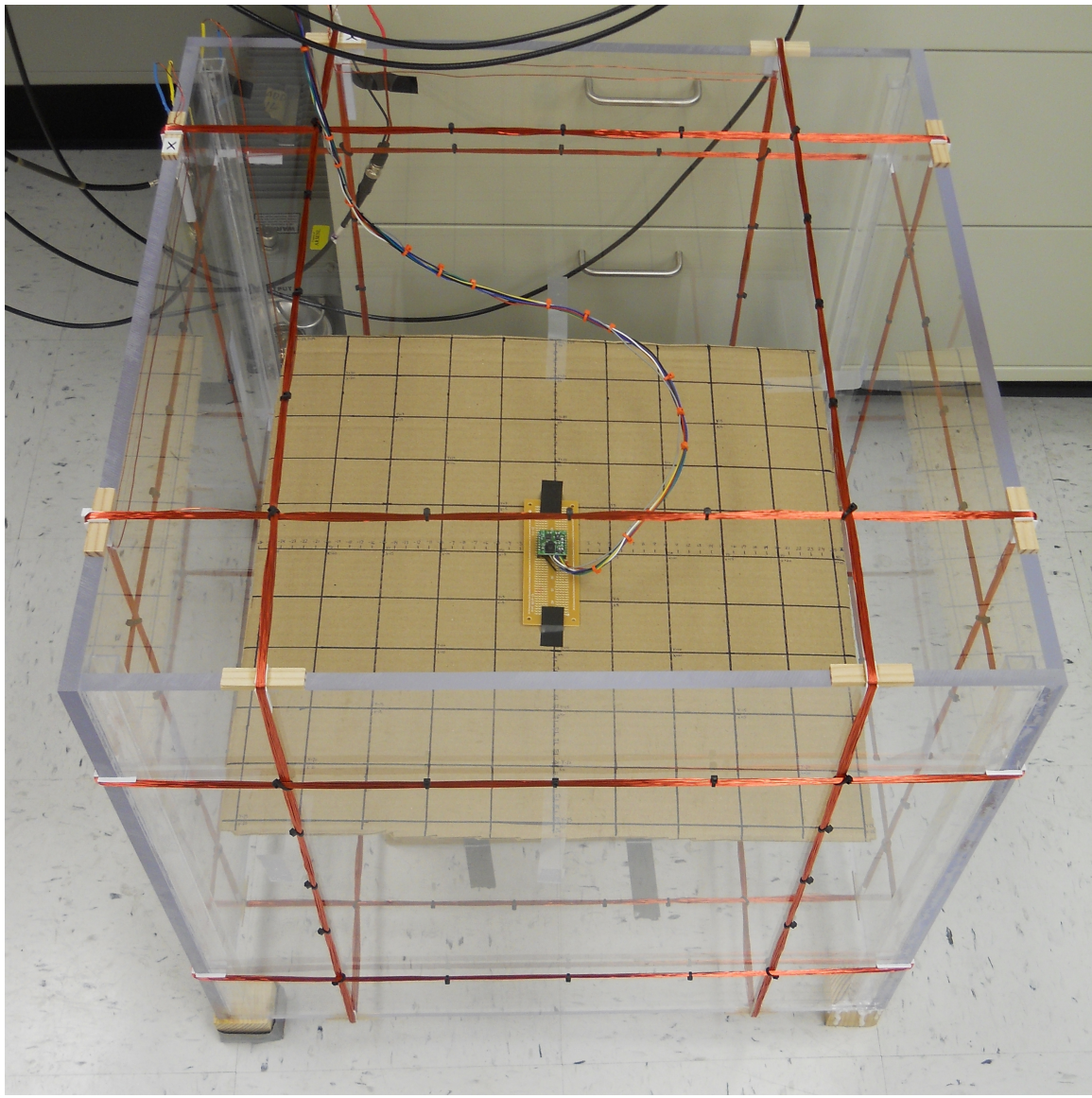


Figure 7.4: The finished Helmholtz cage with side length  $2a=62.23\text{cm}$  and  $h=1.2a=37.24\text{cm}$ . The PNI Micromag 3-axis magnetometer and analysis grid are also shown.



Much of the difficulty involved in the use of a Helmholtz cage is controlling the current output to each coil. Figure 7.5 shows all support hardware and connections necessary for operation of the Helmholtz cage. A PIC18F452 microcontroller is programmed to listen for queries from the serial port and relay the PNI MicroMag 3-axis magnetometer readings when requested. The microcontroller is also responsible for controlling the relay state when commanded via the serial port. Because the programmable power supply is only capable of positive currents, three socket-mounted double pull double throw (DPDT) relays are used to invert the current on each axis as necessary.

A LabView software interface was coded to allow a user to avoid low-level tasks by simply setting a desired constant arbitrary field within the Helmholtz cage. When the software is initializing, it empirically determines the alignment and sensitivity of the magnetometer relative to the Helmholtz cage (described below). After initialization, the software waits for the user to input the desired magnetic field value on each axis. Once the input is collected, the software varies the magnitude and polarity of the current on each axis until the user settings have been achieved.

All magnetic testing described below assumes a constant proportion between current to each coil and the  $H$ -field produced perpendicular to that coil. The “Helmholtz constant” has units of  $\text{m}^{-1}$ , as it represents the magnetizing field ( $\text{A}/\text{m}$ ) per current ( $\text{A}$ ) through the Helmholtz coils. The Helmholtz constant theory is based on Equation 7.5; if  $\mu_0$  and  $I$  are moved to the left side of the equation, the right side is the theoretical Helmholtz constant  $\text{HC}_{\text{theory}}$ . In the center of the Helmholtz cage as built, the theoretical Helmholtz constant  $\text{HC}_{\text{theory}}$  is  $58.8 \pm 0.78 \text{ m}^{-1}$ . This theory-based constant is equivalent on each axis. However, the Helmholtz constant may also be empirically derived through initial calibration. When the LabView software initializes with no hysteresis material present, each axis of the cage is calibrated separately by measuring the magnetic field at two different current values. The empirical calibration constant is then calculated for each axis as follows:

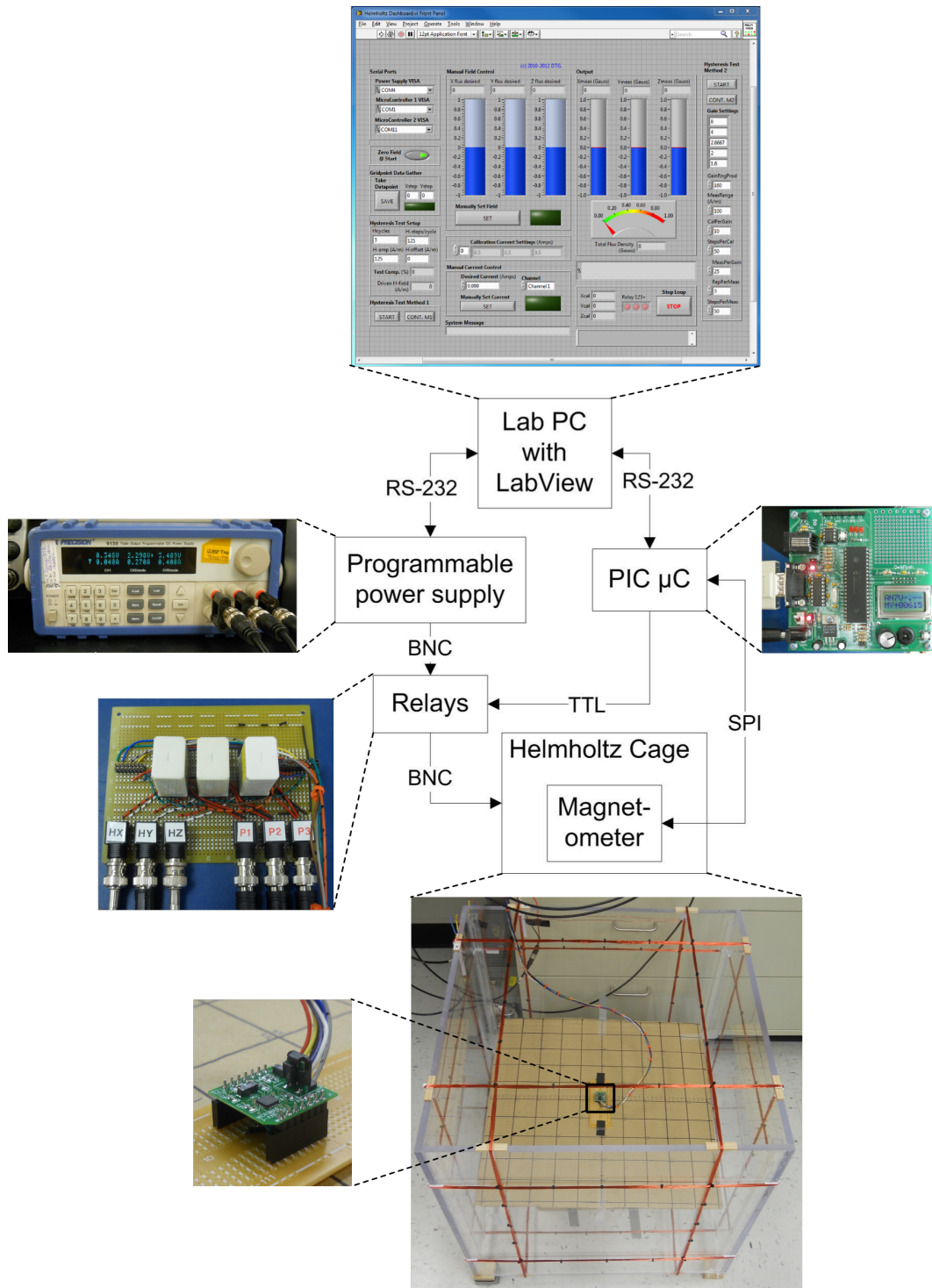
$$\text{HC}_{\text{empirical}} = \frac{B_2 - B_1}{\mu_0(I_2 - I_1)} \quad (7.6)$$

where  $B_1$  is the magnetometer measurement when the coils have current  $I_1$  and  $B_2$  is the magnetometer measurement when the coils current  $I_2$ . The constant  $\mu_0$  is needed because the magnetometer measures the  $B$ -field (not  $H$ -field) within the cage. Testing shows that the empirical Helmholtz constant can change from test to test depending on the alignment of the magnetometer relative to the coils. However, for a properly-aligned, calibrated magnetometer, the empirical Helmholtz constant  $\text{HC}_{\text{empirical}}$  is  $58.8 \pm 0.043 \text{ m}^{-1}$ , which is within the uncertainty bounds of  $\text{HC}_{\text{theory}}$ .

#### 7.1.4 Characterization

Much of the usefulness of the Helmholtz cage depends upon the uniformity of the post-nullification magnetic field within the cage. Thus, the planar field of the Helmholtz cage was mapped using a magnetometer. The magnetometer is used to map a 5cm resolution grid by measuring the total magnetic flux density at each point. This mapping was performed twice: once with no current through the Helmholtz coils and once with the Helmholtz cage set to nullify the local field. Note that the magnetometer is placed in the center of the Helmholtz cage during the nullification process and moved afterward to make the measurements. Figures 7.6a and 7.6b show the magnetic flux density magnitude as a function of planar position. At the time and location of the test, the earth field varied by  $5\mu\text{Tesla}$  over the test area. This caused some variation in the zeroed magnetic field, as shown in Figure 7.6b. As shown, when the Helmholtz cage is zeroed, the test area magnetic field takes the shape of a bowl with a square base: the  $\pm 10\text{cm}$  central area has a measured uniformity of  $2 \mu\text{Tesla}$ , but the field near the edges of the test area reaches  $10 \mu\text{Tesla}$ . The measured field strength variation after field nullification is 5%; this is roughly equivalent to the local field variation before nullification. Repeating the test in a more uniform local field may yield better results. However, a  $20\text{cm} \times 20\text{cm} \times 20\text{cm}$  test volume maintained at  $0\text{-}2\mu\text{Tesla}$  is sufficient for the magnetic testing described later in this chapter. This uniformity was measured for a nullified field but is expected that a Helmholtz-cage-produced arbitrary field of up to  $100 \mu\text{Tesla}$  per axis

Figure 7.5: Helmholtz hardware chain showing signals from the lab computer converted to the appropriate current through the Helmholtz coils.



will possess equivalent uniformity.

## 7.2 Bar Magnet Measurement

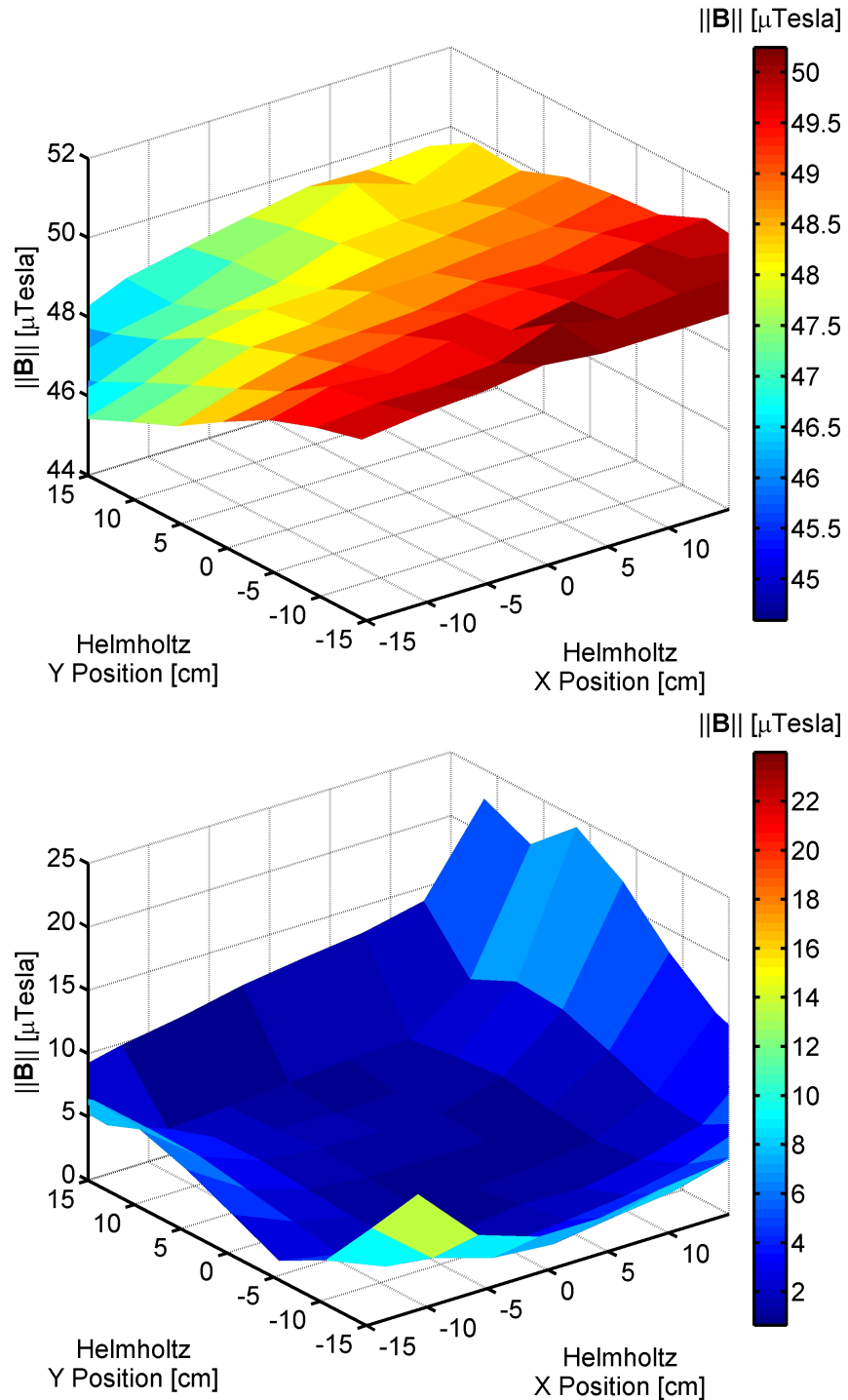
The Helmholtz cage was used to measure the magnetic moment of the bar magnet chosen for use in CSSWE. The steps for the bar magnet measurement are given below:

- (1) Ensure bar magnet is far from Helmholtz cage.
- (2) Take measurement of local magnetic field while magnetometer is at the center of the Helmholtz cage.
- (3) Supply current to the Helmholtz coils to nullify the magnetic field on all three axes. Record the power supply current provided to each axis.
- (4) Using the analysis grid (shown in Figure 7.4), move the PNI MicroMag 3-axis magnetometer, measuring the  $B$ -field magnitude in the 30 cm×30 cm area defined by the grid in steps of 5 cm.
- (5) Place the bar magnet in the center of the analysis grid.
- (6) Again using the analysis grid, record the  $B$ -field magnitude at the same positions as in step (4). Ignore grid positions less than 8cm from the bar magnet position as this may saturate the magnetometer and the dipole model is more accurate with greater distance from the dipole.

Once the two datasets are recorded and corrected for magnetometer calibration error, the  $B$ -field magnitude at each grid position due to the bar magnet alone may be calculated by subtracting the no-bar-magnet data from the bar-magnet data. The measured magnetic flux density magnitude  $\|\mathbf{B}\|_{\text{measured}}$  data are fit to the magnetic dipole magnitude formula using a non-linear least squares fit. The fitted magnetic dipole magnitude equation is [60]:

$$\|\mathbf{B}\|_{\text{measured}} = \left( \frac{\mu_0 m_{\text{fit}}}{4\pi r^3} \right) \sqrt{1 + 3 \cos^2 \nu} \quad (7.7)$$

Figure 7.6: The magnetic flux density magnitude of the Helmholtz cage 30cm×30cm test area is shown with 5cm resolution. The upper plot (a) shows the distribution within the cage when there is no current in the coils; the lower plot (b) shows the distribution when the cage is set to nullify the magnetic field. Note the change in  $B$ -field scaling between a and b.



where  $m_{\text{fit}}$  is the fitted magnetic moment,  $r$  is the distance from the magnet to the measurement location, and  $\nu$  is the magnetic co-latitude of the measurement location ( $90^\circ$  represents a magnetometer position co-planar with the bar magnet position). Three independent measurements were performed, yielding a bar magnet magnetic moment  $||\mathbf{m}|| = 0.80 \pm 0.017 \text{ A}\cdot\text{m}^2$  after a small sample size correction to the standard error of the mean has been applied [33]. Figure 7.7 shows the magnitude of the magnetic flux density and the magnetic dipole fit for the bar magnet measurement data for one of these measurements.

### 7.3 Hysteresis Measurement

The crux of a PMAC system is the hysteresis dampening. It is the most difficult torque to predict and can greatly effect the system settling time. The goal of hysteresis rod magnetic measurement is to determine the relationship between the earth-based  $H$ -field and the magnetic torque due to the hysteresis rods. As explained in Section 2.2.6, a relation from  $H_a$  to  $m$  is sufficient to determine the torque versus the earth's local magnetic field. Equation 2.7 translates the measurement of  $m$  to a measurement of the average magnetic flux density within the rod.

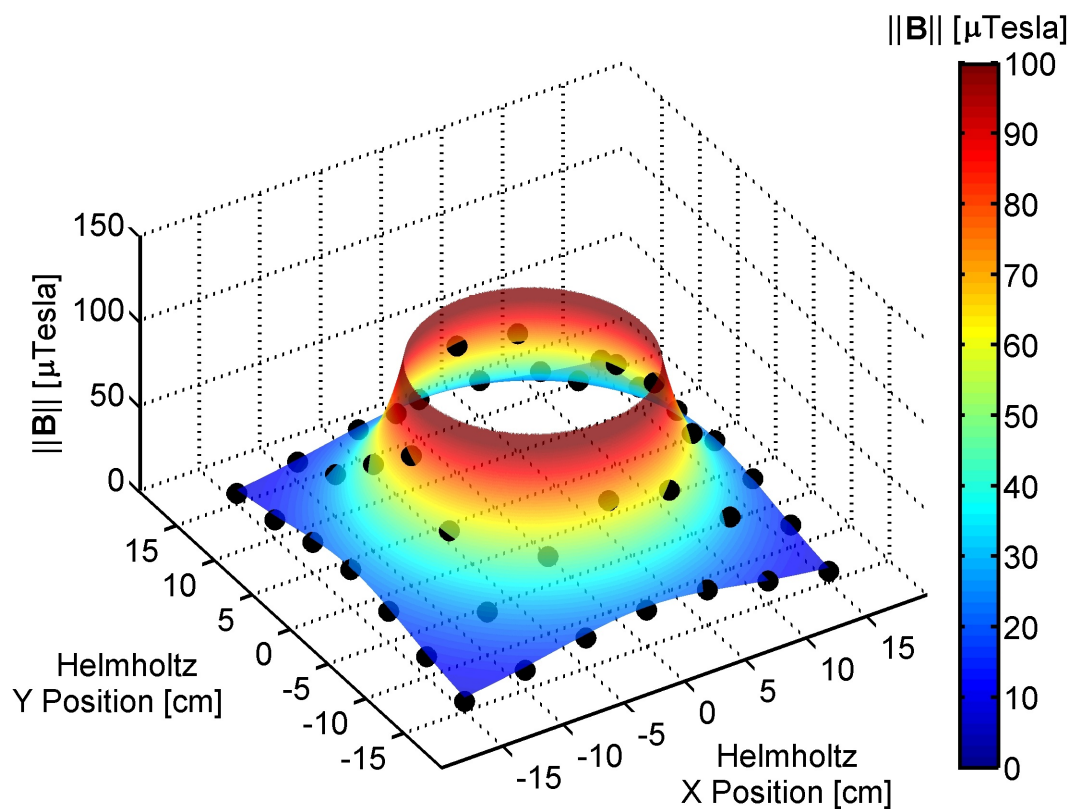
The use of a sense coil within a Helmholtz cage is a novel method of hysteresis rod measurement. The measurement method presented in this section is able to supply a magnetizing field in a large volume and in any direction. This allows multiple samples to be magnetized simultaneously to test their coupled magnetic performance.

#### 7.3.1 Theory

A sense coil connected to an integrator is capable of directly measuring the average interior magnetic flux density of a sample. The Helmholtz cage enables the user to apply a varying magnetizing field over a large test volume. The addition of a sense coil to the Helmholtz cage results in a unique setup which is capable of system-level measurements at a nanosatellite scale.

The theory begins with Faraday's law, which states that a wire coil shall have a voltage generated within it proportional to the rate of change of magnetic flux through the coil [17]:

Figure 7.7: A single bar magnet measurement dataset with the fitted  $0.80 \text{ A}\cdot\text{m}^2$  magnetic dipole overlaid. The  $B$ -field data as recorded by the PNI MicroMag 3-axis magnetometer are shown in black. The magnetic dipole field is shown using the colored surface plot. The dipole field within 8cm of the origin is omitted for clarity.



$$\mathcal{E} = -N \frac{d\phi}{dt} \quad (7.8)$$

where  $\mathcal{E}$  is the voltage induced in the coil,  $N$  is the number of turns of the search coil,  $\phi$  is the magnetic flux in SI units of weber ( $1 \text{ Wb} = 1 \text{ Tesla}\cdot\text{m}^2$ ), and  $t$  is time. Note that voltage is only induced by a changing magnetic flux through the coil. Equation 7.8 may be rearranged and integrated:

$$\int_0^t \mathcal{E} dt = -N \int_{\phi_1}^{\phi_2} d\phi = -N\Delta\phi \quad (7.9)$$

where  $\Delta\phi$  represents the change in  $\phi$ . Because the magnetic flux is directly related to the magnetic flux density by the area of the search coil  $A$ , Equation 7.9 can be written in terms of magnetic flux density:

$$\int_0^t \mathcal{E} dt = -NA\Delta B. \quad (7.10)$$

The integration in Equation 7.10 may be carried out one of two ways: through hardware or software. The hardware method uses an integrator circuit as shown in Figure 7.8. Commercial versions of this circuit (sometimes called a “fluxmeter”) are available for purchase but they were found to be prohibitively expensive. The hardware integrator circuit behaves as follows [17]:

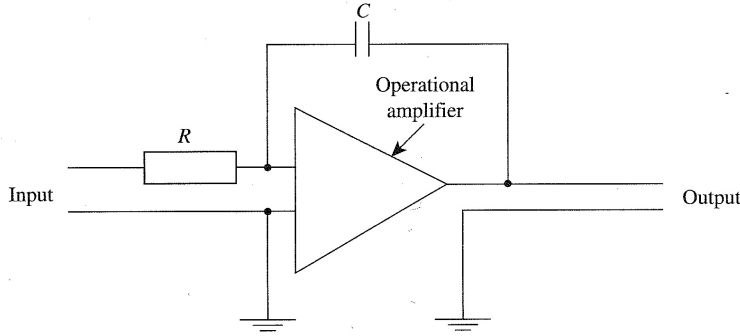
$$\mathcal{E}_{out} = (RC)^{-1} \int_0^t \mathcal{E}_{in} dt \quad (7.11)$$

where  $R$  is the resistor value and  $C$  is the capacitor value. Thus, for a sense coil in series with the integrator:

$$\mathcal{E}_{out} = - \left( \frac{NA}{RC} \right) \Delta B. \quad (7.12)$$

The values of the resistor and capacitor may be calculated based on the materials to be measured. However, after building a hardware-based integrator, we found that temperature- and offset-voltage-based drift made measurements with the hardware integrator difficult. This drift caused the measured hysteresis loops to be significantly distorted and unsuitable for fitting with a hysteresis model. The hardware could be calibrated for one measurement at a time, but the system would drift too much over the course of multiple measurements to be useful for fitting purposes.

Figure 7.8: Hardware integrator circuit for magnetic measurement. Image from Cullity & Graham [17].



A commercial fluxmeter is expensive partially because it is built to correct for these drifts. The implemented low-cost solution is to perform the integration digitally.

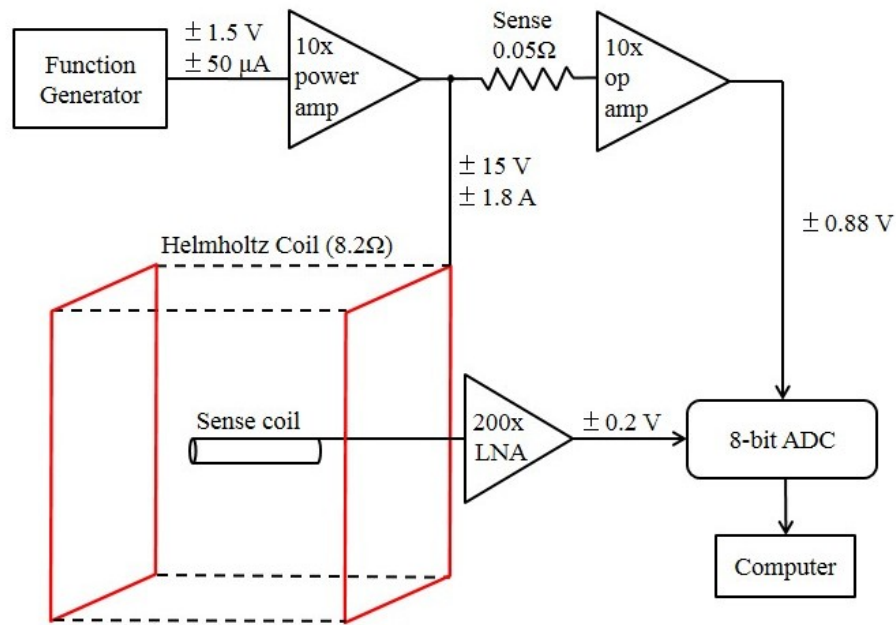
### 7.3.2 Setup

Figure 7.9 is a block diagram of the hardware setup for hysteresis measurement using the Helmholtz cage and a sense coil. Each element of the hardware setup is detailed below.

#### 7.3.2.1 Sense Coil

The magnet wire cannot be wrapped around the hysteresis rod itself due to the minimum bend radius of the magnet wire and the risk of bending the hysteresis rod (thus damaging its magnetic properties). Instead, a sense coil is built such that magnetic samples can be slid within the coil when desired. In order to measure the average B-field of the magnetic sample, the sense coil length should extend the length of the sample. In this case, the sample is the hysteresis rod with a length of  $97.17 \pm 0.03\text{mm}$  and cross-sectional area  $A_m = 0.805 \pm 0.00064 \text{ mm}^3$ . The sense coil is built by tightly winding 36 AWG magnet wire (manufacturer-listed diameter of  $0.1400\text{mm} \pm 0.0013$ ) around a nonmagnetic aluminum tube with an inner/outer diameter of  $5.00/5.30 \pm 0.03\text{mm}$  which yields a cross-sectional sensing area  $A_s = 21 \pm 1.8\text{mm}^2$ . The as-built sense coil (shown within the

Figure 7.9: The hysteresis rod measurement hardware setup block diagram. The labeled voltages and currents are for H-field cycling at  $\pm 100$  A/m amplitude; the amplitude (and subsequent voltages and currents) may be decreased as desired.



Helmholtz cage in Figure 7.10) has a wire-wrapped length of  $96.48 \pm 0.03$  mm; the number of turns is calculated to be  $N = 691 \pm 6$ .

Because the sense coil is wrapped around a hollow tube, the magnetic flux picked up by the sense coil is due to both the magnetic flux through the magnetic material and the magnetic flux through the air surrounding it (yet still within the coil). Thus, the magnetic flux density of each measurement is corrected as follows: [17]

$$B_{\text{true}} = B_{\text{apparent}} - \mu_0 H_a \left( \frac{A_s - A_m}{A_m} \right) \quad (7.13)$$

where  $B_{\text{apparent}}$  is the magnetic flux density as measured via Equation 7.10,  $H_a$  is the applied field,  $A_s$  is the cross-sectional area of the sense coil, and  $A_m$  is the cross-sectional area of the magnetic material.

### 7.3.2.2 Helmholtz Cage

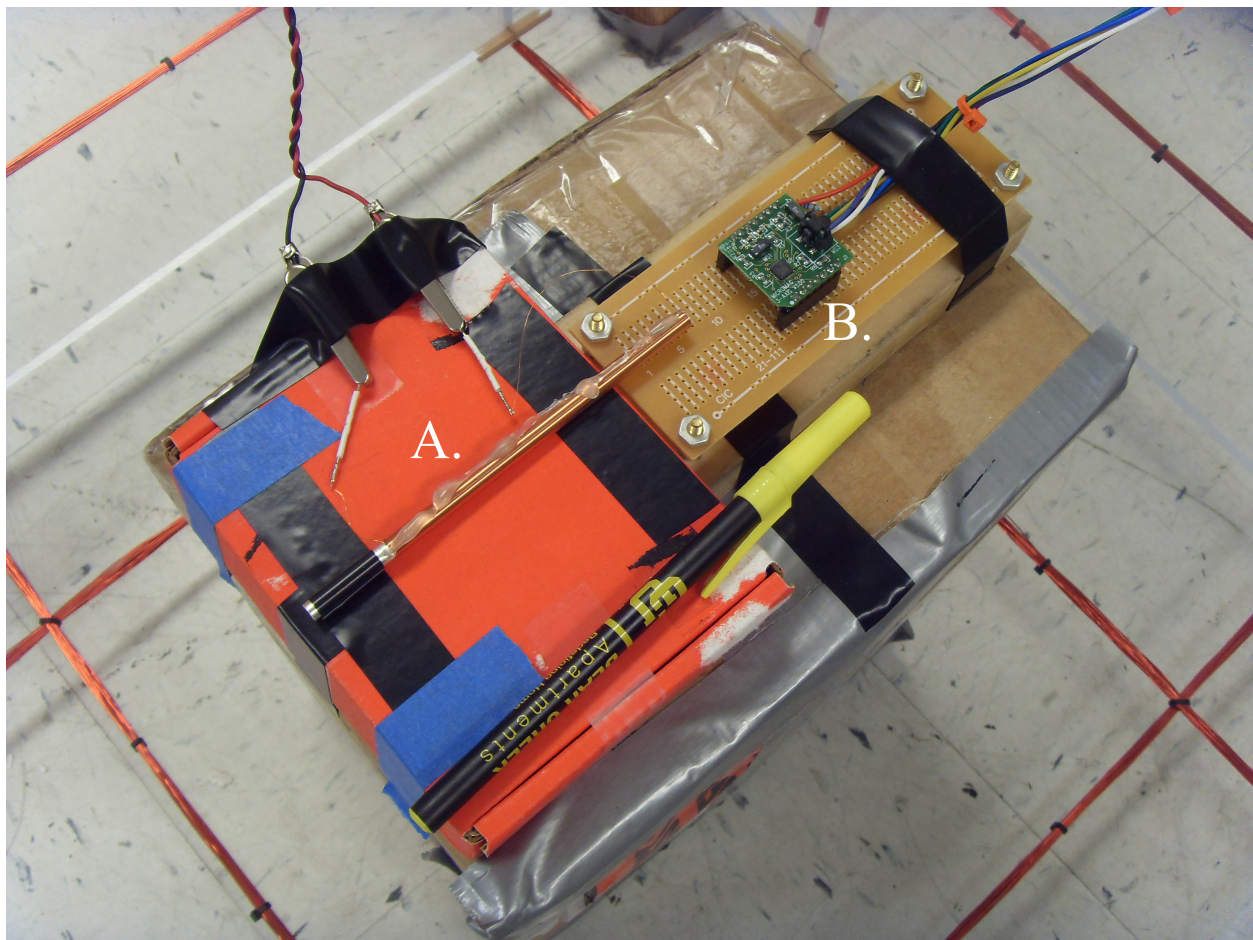
The Helmholtz cage is used to provide the changing magnetizing field strength which causes the magnetic flux density within a magnetic sample to vary. The power supply / relay combination which drives each Helmholtz coil set is capable providing  $\pm 2$  A current with a resolution of  $10 \pm 1$  mA. Using the Helmholtz constant developed in Section 7.1.3, this translates to an ability to control the static magnetizing field (including field nullification) in steps of  $0.59 \pm 0.059$  A/m.

The Helmholtz cage is small enough to allow for orientation changes which can result in improved performance. Before hysteresis rod testing begins, the Helmholtz cage is oriented such that the X-axis is perpendicular to the magnetic field. This allows for testing over the full  $\pm 100$  A/m magnetizing field range which the Helmholtz cage can produce.

### 7.3.2.3 Other Hardware

The Agilent 33220A function generator is used to generate a 1 Hz sine wave with an amplitude of up to  $\pm 1.5$  V for a desired H-field of  $\pm 100$  A/m. This low-current signal is fed to an Apex PA16 power operational amplifier, which multiplies the voltage by a factor of ten while acting as a current

Figure 7.10: The finished hysteresis measurement sense coil (A.) with approximately 691 turns of 36 AWG wire. A pen is shown next to the sense coil for length scale reference; the MicroMag3 3-axis magnetometer (B.) is also visible.



source for a single coil set of the Helmholtz cage. The maximum output current of  $\pm 1.8\text{A}$  supplies an H-field of about  $\pm 100 \text{ A/m}$  to the center of the Helmholtz cage. The supplied H-field is recorded by measuring the voltage generated across a  $50 \pm 0.05 \text{ m}\Omega$  sense resistor. A general-purpose LM741 operation amplifier multiplies the sense resistor output by a factor of ten. Output from the op-amp is digitized by the Picoscope 2205A 8-bit ADC which is set to record a measurement once every  $655.36 \mu\text{s}$ . In many applications, the ADC cannot communicate with the computer fast enough to enable real-time measurements. Instead, the Picoscope has onboard memory with a maximum capacity of 8000 measurements. This means that the Picoscope can measure about 5.25 cycles at 1 Hz before stopping to send the dataset to the computer. The Picoscope has two inputs which it can measure nearly simultaneously and has a triggering feature which ensures that all measurements begin at the same phase of the H-field cycle.

The sense coil output is multiplied by a dual INA2126 low-noise operational amplifier. The first amplification is a factor of 100, the second is a factor of two. After this amplification, the typical signal from the tested hysteresis rod given  $\pm 100 \text{ A/m}$  is about  $\pm 200\text{mV}$ . This output is fed to the Picoscope ADC which digitizes the data for the computer.

### **7.3.3      Method**

The hysteresis rod measurement method as performed by the user is outlined below.

- (1) Orient Helmholtz cage such that one axis is perpendicular to the local magnetic field.
- (2) Ensure no magnetic material is present in the Helmholtz cage test volume.
- (3) Place magnetometer in center of Helmholtz cage and align to Helmholtz cage axes (the magnetometer may be used to determine if the cage is properly aligned relative to the magnetic field).
- (4) Ensure that all axes of the Helmholtz cage are connected to the computer-controlled power supply outputs. The function generator / power amp output should not be connected yet.

- (5) Initialize the LabVIEW-based Helmholtz cage software. The software will now calculate the Helmholtz constant  $HC_{\text{empirical}}$ .
- (6) Set the software to nullify the magnetic field on all three axes. If the Helmholtz cage is properly aligned, zero current should be needed to nullify the field on one of the axes.
- (7) Detach the power supply output from the coil set which is perpendicular to the B-field. Attach this coil set to the function generator / power amp output.
- (8) Enable the function generator at 1 Hz and enable the power amp. The magnetometer output should show varying magnetic field along a single axis.
- (9) Remove the magnetometer from the Helmholtz cage. Place the sense coil perpendicular to the zero-current coil set.
- (10) Set the function generator to the desired output voltage, being careful not to exceed 1.5V.
- (11) Collect one 8000-point dataset.
- (12) Place the magnetic sample within the sense coil being careful not to disturb the orientation of the coil.
- (13) Collect one 8000-point dataset.
- (14) Repeat steps 10-13 until all samples have been measured at all desired H-field amplitudes.

The list above simply describes the physical process of collecting a hysteresis measurement; analysis occurs thereafter. Figure 7.11 shows a block diagram of the analysis process after collecting the digital dataset. The H-field is processed by removing the 10x amplification, converting to current, and multiplying by  $HC_{\text{empirical}}$ . The B-field measurement is more complicated. After removing the gain of the signal, the signal due to the changing flux of the local environment is removed by subtracting the measurement without the sample from the measurement with the sample. After background subtraction, the data is numerically integrated using the trapezoidal

method. The integrated voltage is converted to the B-field by application of Faraday's Law. The constant offset after numeric integration is determined by assuming that the hysteresis loop is symmetric; the constant offset of a linear fit to the hysteresis loop is removed from all B-field values.

The data is bifurcated into two distinct groups: data from the top/bottom hysteresis curves. The data grouping is based on whether the B-field is rising or falling (the sine wave behavior makes this easy to characterize). Further processing is possible due to the length of the each dataset (over five H-field cycles) and the digitization of the H-field measurements. The H-field resolution of the 8-bit ADC varies from 0.105 A/m ( $\pm 10$  A/m) to 1.04 A/m ( $\pm 100$  A/m). Thus, the measurements are further grouped into various B-field values at each unique H-field value and curve. The B-field average and standard deviation are calculated for the unique H-field values of each curve. This provides an estimate of the B-field uncertainty and is useful for further data processing.

#### 7.3.4 Results

Two types of hysteresis measurements are performed: isolation and system testing. Isolation testing measures hysteresis rod performance with no other magnetic materials nearby. System testing measures the hysteresis rod performance with a bar magnet and other hysteresis materials distributed identically to the flight satellite. In each measurement type, a nonlinear weighted least-squares fit is used to determine the hysteresis parameters ( $H_c$ ,  $B_r$ , and  $B_s$ ) which best match the data. The data are weighted by the inverse of their uncertainty and the Flatley [26] hysteresis model (described in Section 8.1.6.5) is used for the fit. Figure 7.12 shows one such  $\pm 100$ A/m cycle amplitude dataset with its parameter-based fitted hysteresis loop.

Each experimental dataset was independently measured two times and independently fit to the Flatley model to develop an uncertainty estimate of the mean fit parameters. A small sample size correction to the standard error of the mean is applied to each of the uncertainty estimates [33]. Five CSSWE flight spare hysteresis rods were available for measurement. The measurement is performed after the launch of CSSWE and uses hysteresis rods from the same raw material order

Figure 7.11: Hysteresis measurement analysis block diagram. The top (A.) and bottom (B.) rectangles highlight the analysis procedure for the H-field and B-field, respectively. Multiplication is denoted by a triangle, subtraction is denoted by a rounded rectangle, and integration is denoted by a diamond.

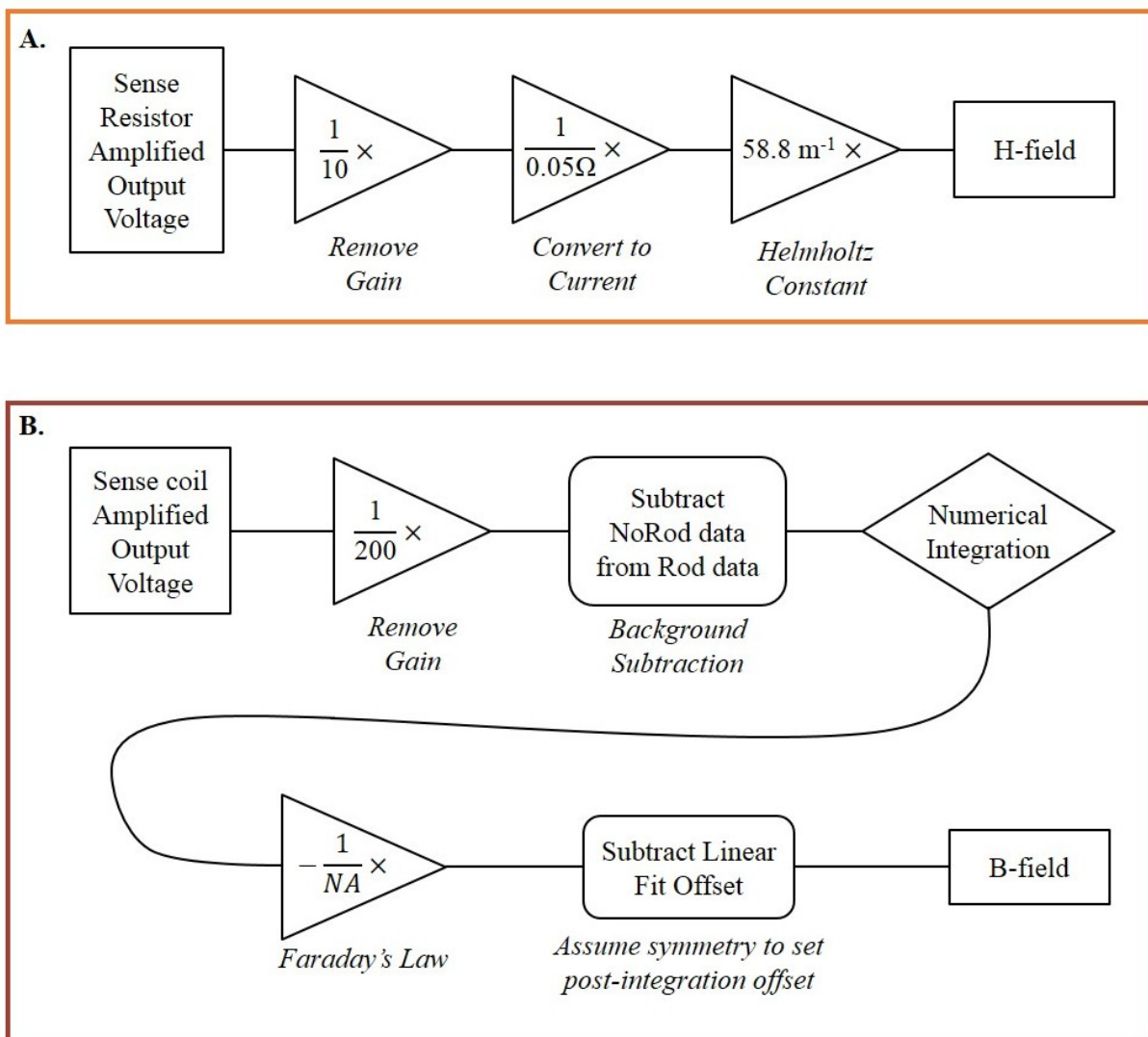
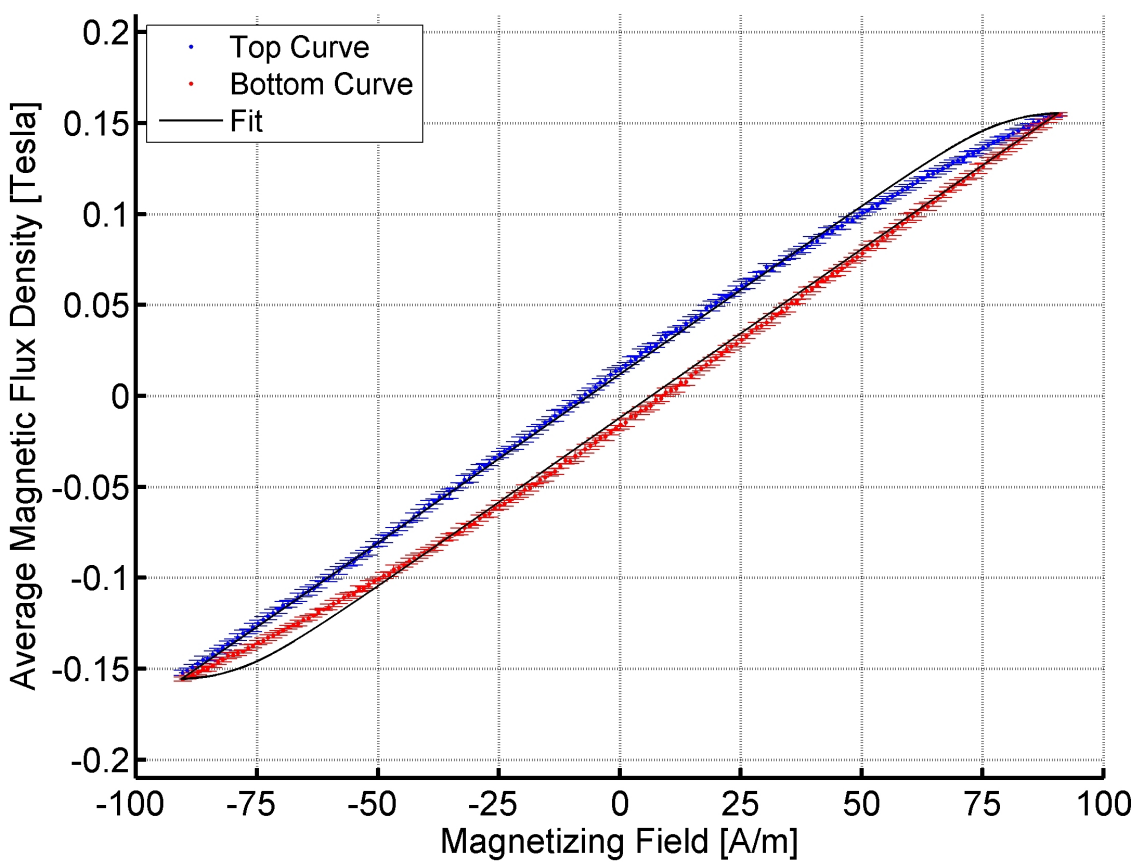


Figure 7.12: The  $\pm 100\text{A/m}$  cycle amplitude measurement dataset of rod B with its fitted hysteresis loop. Error bars are included for each averaged flux density measurement.



and heat treatment set as the flight rods used on orbit.

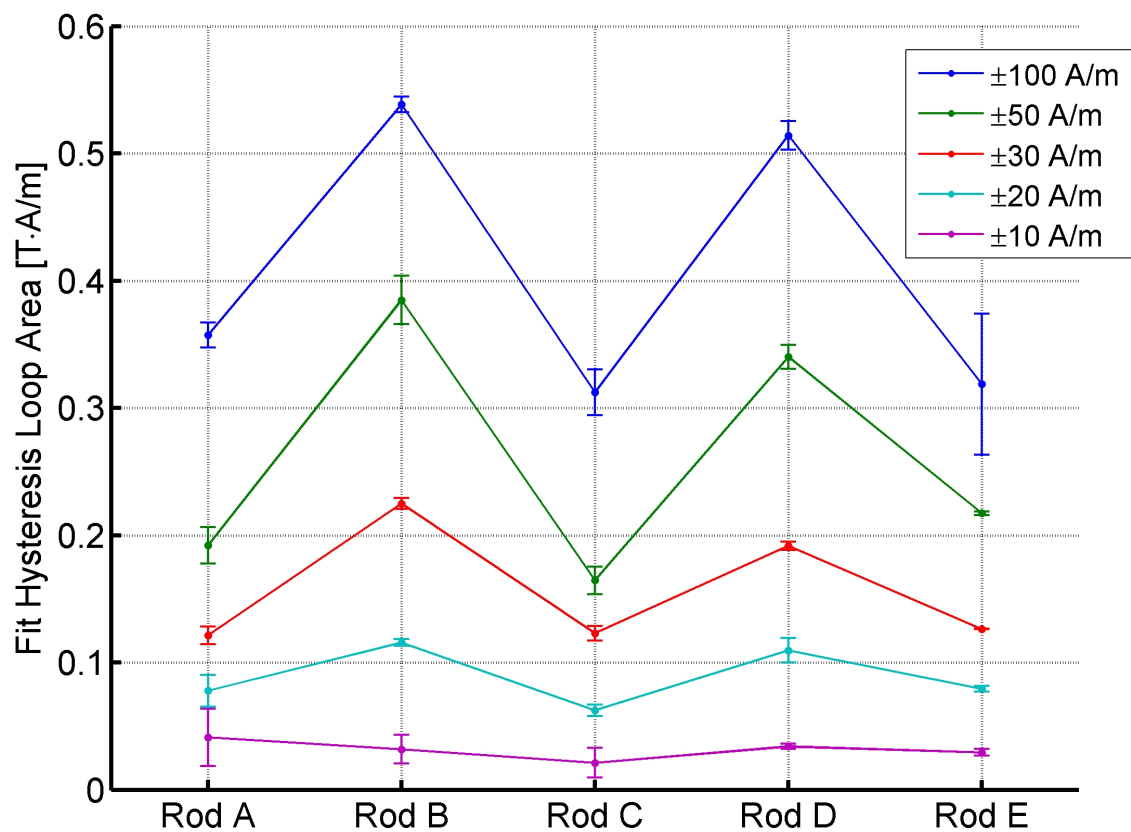
#### **7.3.4.1 Isolated Measurement**

Each isolated rod measurement was fitted separately at each H-field cycle amplitude. The area of each simulated fit loop for each measurement is shown in Figure 7.13. The area of each simulated fit loop is calculated using an H-field cycle amplitude of  $\pm 20$  A/m. Note that the product of the hysteresis loop area and the hysteresis rod volume is the energy loss per H-field cycle. Thus, the dampening ability of each rod varies significantly. Surprisingly, the simulated  $\pm 20$  A/m loop area of each fit also varies significantly depending on the H-field cycle amplitude during the empirical measurement.

If the hysteresis model behaved perfectly, fit parameters based on a variety of empirical H-field cycle amplitudes would yield identical simulated cycle loop areas at the same simulated cycle amplitude. Figures 7.15 and 7.16 compare the hysteresis loops generated from a variety of simulated cycle amplitudes given hysteresis parameters fit data measured from  $\pm 100$  and  $\pm 10$  A/m empirical cycle amplitudes, respectively. The simulated loop areas for each fit at identical simulated cycle amplitudes are quite different. The fitted parameters best represent the true hysteresis loop when the measurement magnetizing field cycle amplitude is close to the simulated cycle amplitude. Thus, to achieve accurate simulation results, the measurement cycle amplitude should equal the range of magnetizing field which the true hysteresis rod is expected to experience the most frequently during dampening.

The extremes of the magnetization cycle amplitude are bounded by the magnitude of the on-orbit H-field but the extremes of the H-field component parallel to each rod will vary as the satellite attitude settles. Figure 7.14 shows the magnetizing field parallel to the hysteresis rods mounted along the  $^B X$  and  $^B Y$  axes. As shown, CSSWE experienced magnetizing field cycle amplitudes from  $\pm 40$  A/m to less than  $\pm 5$  A/m within the first seven days after launch. Note that smaller cycles due non-flat-spin motion occur but are difficult to see in this plot. For this reason, the fitted hysteresis parameters used by the simulation are based on measurement cycle amplitudes of  $\pm 20$

Figure 7.13: The simulated  $\pm 20$  A/m hysteresis loop area for hysteresis parameters fitted to a variety of H-field cycle amplitude datasets gathered for each of five measurement hysteresis rods. Each measurement was recorded with no other magnetic materials nearby.



and  $\pm 10$  A/m; these values are chosen in an attempt to use the most frequent cycle amplitudes experienced by each hysteresis rod during the settling period.

Figures 7.15 and 7.16 also show that the  $\pm 100$  A/m model degrades at especially small cycle amplitudes: each cycle is no longer a closed loop. This behavior is unrealistic and undesired. The parameters from the  $\pm 10$  A/m cycle perform much better at these low magnetizing field levels. Correctly representing these small cycle amplitudes is important because these loops are regularly encountered due to non-flat-spin motion throughout dampening. This is another reason to use a low cycle amplitude during measurement.

#### **7.3.4.2 System-based Relative Position Measurement**

The layout of PMAC components within a satellite may impact the dampening ability of each hysteresis rod. The net effect of the layout may be measured by placing magnetic components in their relative satellite positions and measuring individual hysteresis rod performance. Rods C, D, E, and F were placed at the X2, X3, Y2, and Y3 hysteresis rod positions within a CSSWE flight structure mock-up (see Figure 5.2). A flight spare bar magnet was also added to the mock-up in the flight position. The sense coil was then used to measure the performance of rod A at each of the hysteresis rod positions; the native rod at each position was removed during the measurement. Figure 7.17 shows the full setup for this measurement while Figure 7.18 shows the simulated area of the fitted hysteresis parameters.

There is some variation but the difference is only significant for the  $\pm 100$  A/m cycle amplitudes case. The hysteresis rod positions closest to the bar magnet (X3 and Y3) could be expected to possess decreased dampening abilities due to their increased H-field offset. The data shows that, for the CSSWE layout, interactions between rods are more important than the offset due to the bar magnet. Figure 7.19 shows the calculated H-field parallel to each rod position due to an  $0.80$  A·m<sup>2</sup> dipole aligned with  $+^BZ$  at the bar magnet location. Although the rods each experience a magnetizing field variation of up to  $4.5$  A/m along their length, the average H-field offset is 1-2 A/m.

Figure 7.14: The magnetizing field experienced by each of the body-frame axes with parallel hysteresis rods ( ${}^B X$  and  ${}^B Y$ ) over the first week on-orbit. Each hysteresis rod experiences a wide variety of H-field cycle amplitudes.

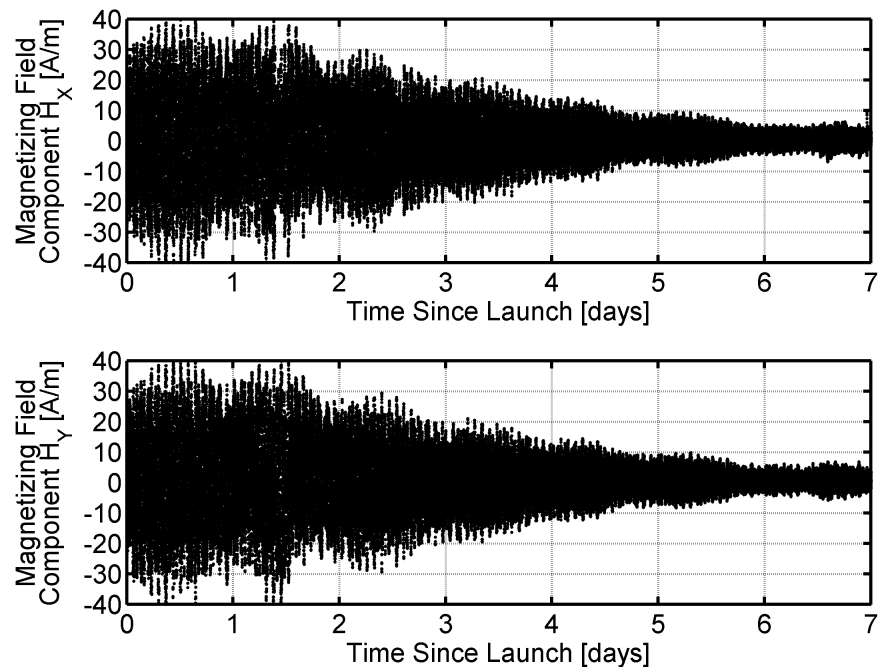


Figure 7.15: A variety of simulated hysteresis loops generated using parameters fitted to measured output from an empirical cycle amplitude of  $\pm 100$  A/m. Each H-field amplitude is used to simulate 10 cycles of data. The top plot shows the simulated performance at bounds of  $\pm 10$  A/m; the bottom plot zooms to show the same data at a range of  $\pm 2$  A/m.

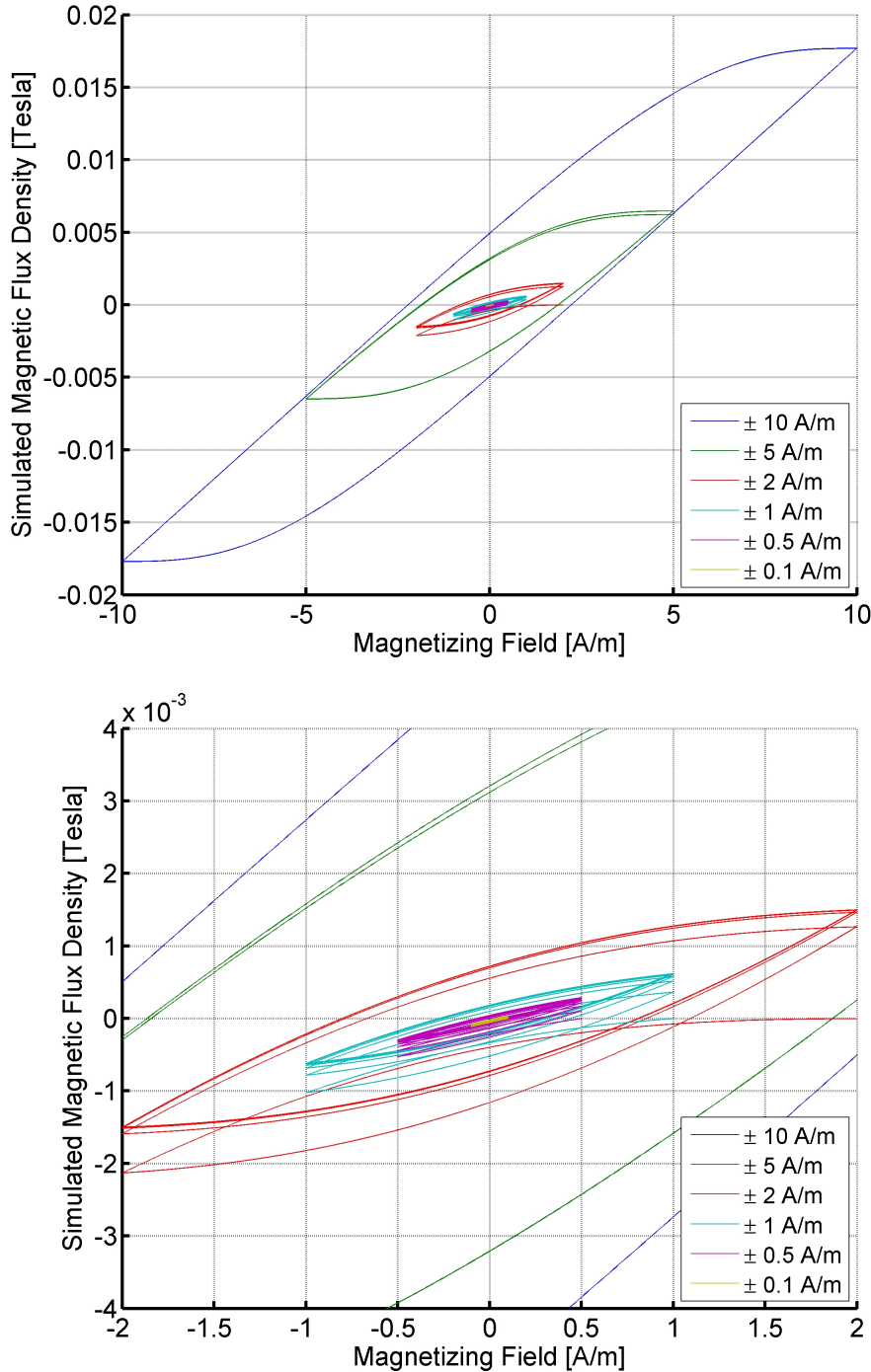


Figure 7.16: A variety of simulated hysteresis loops generated using parameters fitted to measured output from an empirical cycle amplitude of  $\pm 10$  A/m. Each H-field amplitude is used to simulate 10 cycles of data. The top plot shows the simulated performance at bounds of  $\pm 10$  A/m; the bottom plot zooms to show the same data at a range of  $\pm 2$  A/m.

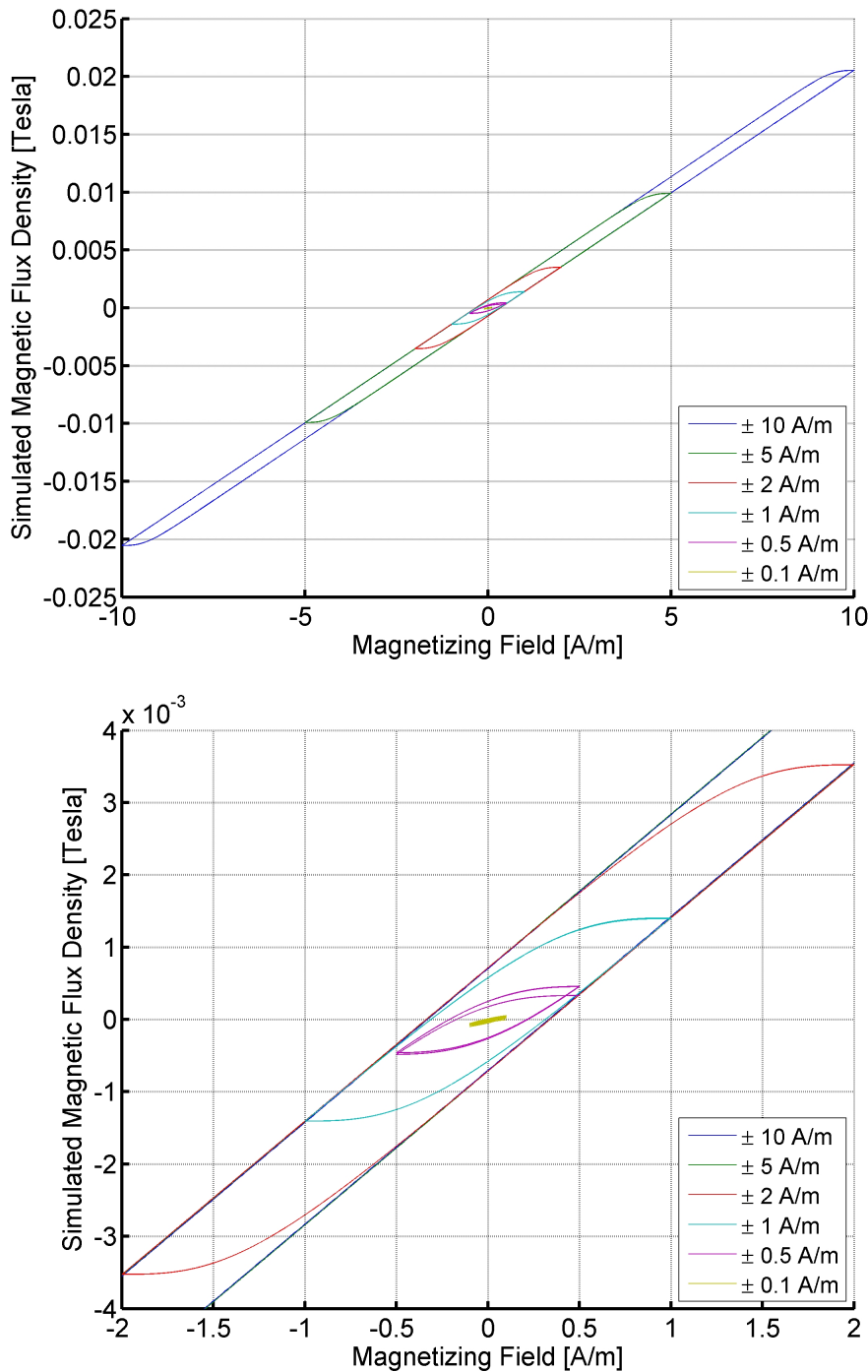


Figure 7.17: The CSSWE flight structure mock-up with hysteresis rods and bar magnet attached is used to measure the effect of other magnetic sources on a single hysteresis rod. The sense coil is in the X3 position (as defined by Figure 5.2).

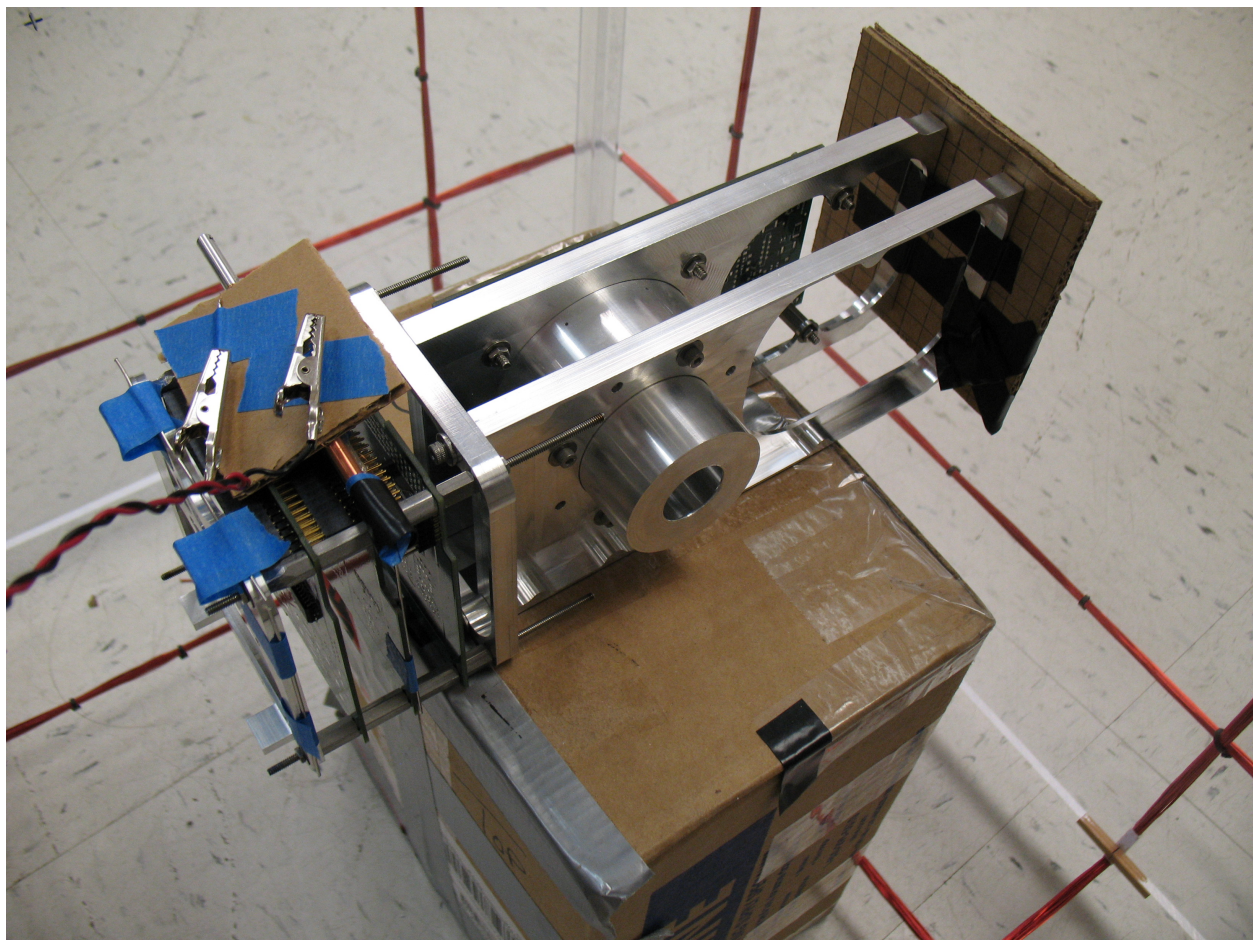


Figure 7.18: The simulated hysteresis loop area using hysteresis parameters fitted to Rod A measurements performed at a variety of cycle amplitudes. The measurements are collected at each of the X2, X3, Y2, and Y3 hysteresis positions labeled in Figure 5.2. The Rod A Isolated Testing results are repeated here for comparison.

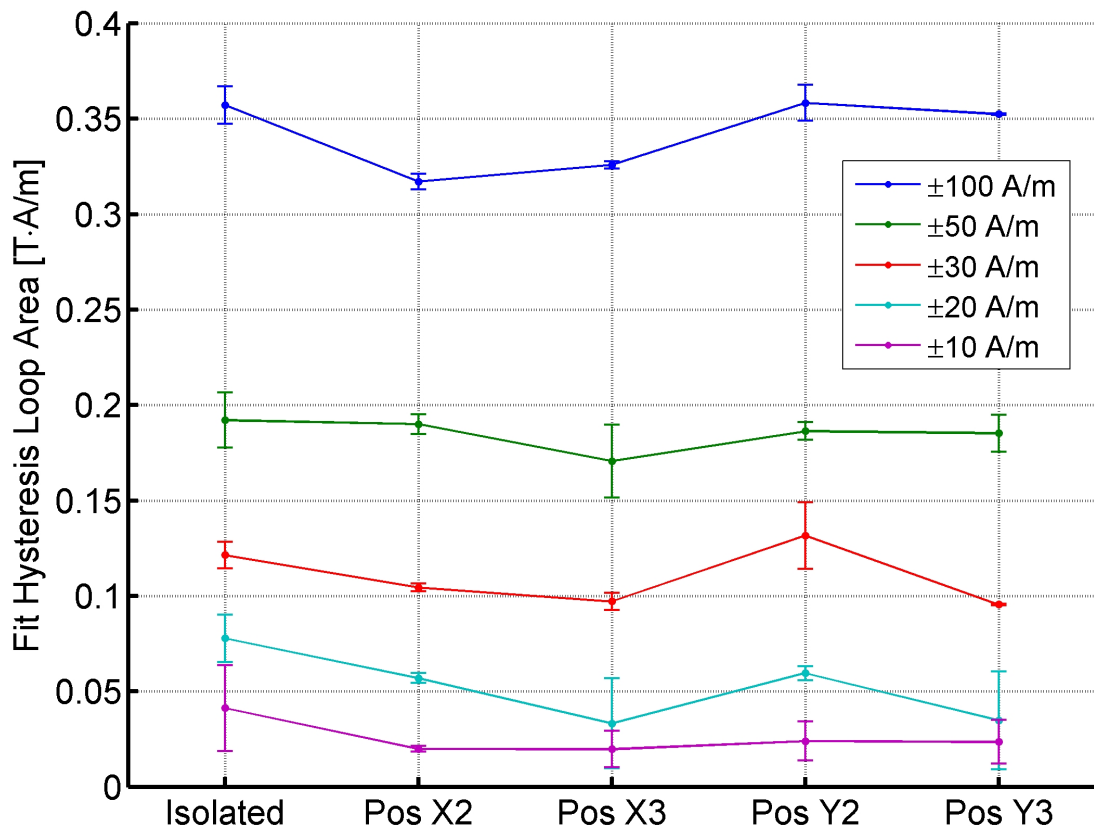


Figure 7.19: The magnetizing field offset parallel to each hysteresis rod position due to an  $0.80 \text{ A}\cdot\text{m}^2$  dipole aligned with  $+^BZ$  at the bar magnet location. The value of the mean H-field parallel to each rod is shown using open circles.

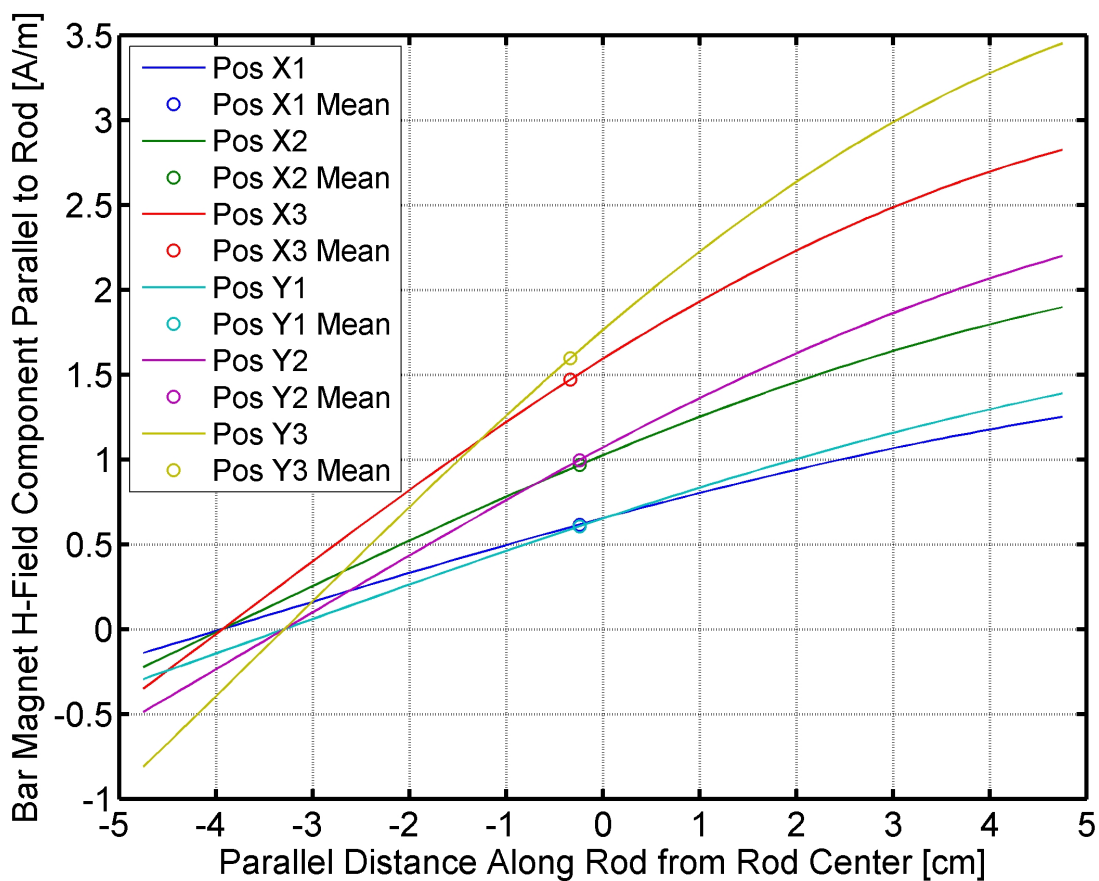


Table 7.2: HyMu-80 Hysteresis Parameters. The area was calculated using the Flatley hysteresis model [26] with a cycle amplitude of  $\pm 20$  A/m.

Hysteresis Parameter	Closed Magnetic Circuit Value (Material Datasheet)	Open Magnetic Circuit Value (Fitted to Measurement)
$H_c$ (A/m)	1.59	0.3381
$B_r$ (Tesla)	0.35	$6.0618 \times 10^{-4}$
$B_s$ (Tesla)	0.73	0.3000
Loop Area ( $J \cdot m^{-3}$ )	4.312	0.0448

#### 7.3.4.3 Best-Fit Hysteresis Parameters

The individual testing shows that the hysteresis rod dampening ability varies significantly for each rod. However, the system testing shows that the position of a given rod within the CSSWE layout does not have a significant effect on the dampening ability of the rod at cycle amplitudes less than  $\pm 50$  A/m. Also, the hysteresis model has been found to work best when simulating data closest to its measurement cycle amplitude. To simplify the simulation, one set of parameters is used to model all six hysteresis rods within CSSWE. With all of the above considerations in mind, the best-fit parameters are found by fitting the individual measurement data from all five hysteresis rods over both tests at magnetizing field cycle amplitudes of both  $\pm 10$  and  $\pm 20$  A/m.

The fitted hysteresis loop parameters are collected in Table 7.2 and compared to the closed magnetic circuit values listed for the rod material. Note that the datasheet-based hysteresis parameters yield a loop area nearly 100 times greater than the measurement-based values. This difference in hysteresis dampening ability will have the profound effect of changing the simulated settling time by the same factor.